

Open access • Journal Article • DOI:10.1038/NATURE13681

Gradual unlocking of plate boundary controlled initiation of the 2014 Iquique earthquake — Source link 🔼

Bernd Schurr, Guenter Asch, Sebastian Hainzl, Jonathan Bedford ...+12 more authors

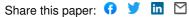
Institutions: Peking University, University of Chile, Institut de Physique du Globe de Paris

Published on: 21 Aug 2014 - Nature (Nature Research)

Topics: Interplate earthquake, Foreshock, Seismic gap, Intraplate earthquake and Seismic hazard

Related papers:

- Intense foreshocks and a slow slip event preceded the 2014 Iquique Mw 8.1 earthquake
- Continuing megathrust earthquake potential in Chile after the 2014 Iquique earthquake
- · Reappraisal of great historical earthquakes in the Northern Chile and Southern Peru seismic gaps
- Slab1.0: A three-dimensional model of global subduction zone geometries
- The 1 April 2014 Iquique, Chile, Mw 8.1 earthquake rupture sequence











Originally published as:

Schurr, B., Asch, G., Hainzl, S., Bedford, J., Hoechner, A., Palo, M., Wang, R., Moreno, M., Bartsch, M., Zhang, Y., Oncken, O., Tilmann, F., Dahm, T., Victor, P., Barrientos, S., Vilotte, J.-P. (2014): Gradual unlocking of plate boundary controlled initiation of the 2014 Iquique earthquake. - *Nature*, *512*, p. 299-302

DOI: http://doi.org/10.1038/nature13681

Gradual unlocking of plate boundary controlled initiation of the 2014 Iquique earthquake

Bernd Schurr¹, Günter Asch¹, Sebastian Hainzl¹, Jonathan Bedford¹, Andreas Hoechner¹, Mauro Palo¹, Rongjiang Wang¹, Marcos Moreno¹, Mitja Bartsch¹, Yong Zhang², Onno Oncken¹, Frederik Tilmann¹, Torsten Dahm¹, Pia Victor¹, Sergio Barrientos³, Jean-Pierre Vilotte⁴

On April 1st, 2014, Northern Chile was struck by a magnitude 8.1 earthquake following a protracted series of foreshocks. The Integrated Plate boundary Observatory Chile (IPOC) monitored the entire sequence of events, providing unprecedented resolution of the build-up to the main event and its rupture evolution. Here we show that the Iquique earthquake broke a central fraction of the so-called Northern Chile seismic gap, the last major segment of the South American plate boundary that had not ruptured in the past century^{1,2}. Since July 2013 three seismic clusters, each lasting a few weeks, hit this part of the plate boundary with earthquakes of increasing peak magnitudes. Starting with the second cluster, geodetic observations show surface displacements that can be associated with slip on the plate interface. These seismic clusters and their slip transients occupied a part of the plate interface that was transitional between a fully locked and a creeping portion. Leading up to this earthquake the b-value of the foreshocks gradually dropped during the years prior to the earthquake, reversing its trend a few days before the Iquique earthquake. The main shock finally nucleated at the northern end of the

¹ GFZ Helmholtz Centre Potsdam, German Research Centre for Geosciences, Telegrafenberg 14473 Potsdam, Germany,

² School of Earth and Space Sciences, Peking University, Beijing 100871, China,

³ Centro Sismologico National, Universidad de Chile, Facultad de Ciencias Físicas y Matemáticas, Blanco Encalada 2002 - Santiago, Chile,

⁴ Institut de Physique du Globe de Paris, 1, rue Jussieu - 75238 Paris cedex 05, France

foreshock area, which skirted a locked patch, and ruptured mainly downdip towards higher locking. Peak slip was attained immediately down-dip of the foreshock region and at the margin of the locked patch. We conclude that gradual weakening of the central part of the seismic gap accentuated by the foreshock activity in a zone of intermediate seismic coupling was instrumental in causing final failure, distinguishing the Iquique earthquake from most great earthquakes. Finally, only one third of the gap was broken and the remaining locked segments now pose a significant, increased seismic hazard with the potential to host an earthquake of >M 8.5.

The Northern Chile Southern Peru seismic gap last broke in 1877 in a great earthquake (Mw≈ 8.8)¹ rupturing from south of Arica to the Mejillones Peninsula (see Fig. 1). The reported historical recurrence interval for the past 500 years in this region has been estimated at 111 +/- 33 years¹ likely making it the most mature seismic gap along the South American plate boundary. In the past two decades the two adjoining segments south and north broke in the Mw 8.1 Antofagasta earthquake of 1995³,⁴ and the Mw 8.4 Arequipa earthquake of 2001 in southern Peru⁵. In the previous cycle the southern Peru and Northern Chile segments broke within few years (Fig. 1), suggesting that they might be coupled in time¹. The imminence of a large megathrust event in this region motivated the setup of an international monitoring effort with the Integrated Plate Boundary Observatory Chile (IPOC). Having started in 2007, there now exists an exceptional database that monitors the gradual plate boundary failure with various geophysical techniques.

Several major earthquakes (Mw>7) have occurred in this gap since 1850 (Fig. 1); the largest until now was the Mw 7.7 Tocopilla earthquake in 2007, which broke the southern rim of this segment beneath and north of Mejillones Peninsula along a total length of 150 km. Only the downdip end of the locked zone slipped in this event, and the total slip in the rupture area was less than 2.6 m^{6,7} leaving most of the past slip deficit of c. 8-9 m accumulated since 1877

unaffected⁸. On April 1st, 2014, the Mw 8.1 Iquique earthquake north of Iquique struck the central portion of the gap. Using seismological and geodetic observations we here analyze the rupture, its relationship to previous locking of the plate interface, as well as the pre-seismic transients leading up to the earthquake.

Kinematic analysis of the Mw 8.1 Iquique rupture makes use of two complementary approaches. First, we performed waveform modelling of local strong motion seismograms and teleseismic body waves to constrain the kinematic development of the rupture towards the final displacement in a joint inversion with continuous GPS data of static displacements (Fig. 1, 2a). Second, we use the backprojection technique applied to stations in North America to map the radiation of high frequency seismic waves (HFSR; 1-4 Hz)^{9,10}. The latter technique is not sensitive to absolute slip amplitudes, but rather to changes in slip and rupture velocity. During the first 35-40s the rupture propagated downdip with increasing velocity, nearly reaching the coastline (Fig. 2a,b). Surprisingly, towards the end of the rupture, the area near the epicenter was reactivated. In spite of the relatively complicated kinematic history of the rupture the cumulative slip shows a simple 'bull's eye' pattern with a peak coseismic slip of about 4.4 m (Fig. 1), consistent with Lay et al.'s 11 slip model based on teleseismic and deepwater tsunami wave recordings. Yagi et al. 12 find a slip patch of similar size and magnitude but with the highest slip placed ~40 km further south from teleseismic only recordings, which, however, appears not compatible with onshore displacement measurements from GPS. The largest aftershock so far was the Mw 7.6 event of April 3rd that, like the main shock, ruptured initially downdip. Rupture then propagated northeastward, attaining a peak slip of 1.2 m after about 20s. Both earthquakes broke a total of 200 km of the margin.

The Iquique rupture affected an area shown from geodetic analysis to be a zone of intermediate interseismic coupling at 18.5-21°S interrupting the otherwise fully locked Northern Chile Southern Peru gap^{8,13} (Fig. 3a). The Iquique main shock nucleated at the

northwestern border of a locked patch and ruptured towards its center (Fig. 2a, 3a). The downdip end of the main shock as well as for the large Mw 7.6 aftershock rupture mapped both by the HFSR and co-seismic slip agrees quite accurately with the downdip end interseismic coupling (Fig. 2a,c 3a). The accelerated downdip rupture propagation for both earthquakes closely followed the gradient towards higher locking. Therefore, the Iquique event and its largest aftershock appear to have broken the central, only partly locked segment of the Northern Chile Southern Peru seismic gap releasing part of the slip deficit accumulated here since 1877 (cf. Fig. 1).

The seismicity before the Iquique earthquake also concentrates in this zone of intermediate locking at the fringe of the highly locked – high slip patch (Fig. 3a). Starting in July 2013, three foreshock clusters with increasingly larger peak magnitudes and cumulative seismic moment occurred here (Fig. 2c, 3a,c). The mainshock rupture started at the northern end of the foreshock zone, inside the region of intermediate locking (Fig. 2c, 3a). Interestingly, the second foreshock cluster (January 2014) is associated with a weak transient deformation, whereas the third cluster (March 2014) shows a very distinct transient signal. GPS displacement vectors calculated over the times spanning these foreshock clusters point towards the cluster epicentres (Extended Data Figure 4). Deformation for both transients is entirely explained by the cumulative coseismic displacement of the respective foreshock clusters (Fig. 3d inset, Extended Data Figure 4). The area affected by the foreshocks is then reactivated by the aftershock sequence of the Iquique earthquake (Fig. 2c). Comparing this to the long term deformation history of the margin, we find that the same area exhibits a high gradient of locking from weakly locked updip to fully locked downdip (Fig. 3a).

Additionally, the analysis of the frequency-magnitude distribution of the foreshocks reveals outstanding characteristics in both the spatial and temporal vicinity of the rupture. The earthquake number N as a function of the magnitude M is found to follow the well-known

Gutenberg-Richter relation, $N \sim 10^{-bM}$. b-values have been proposed to act as stress-sensor with low b-values indicating high stresses¹⁴. Mapping the b-value in Fig.3b indicates significantly lower b-values in the source area compared to all other regions where the b-value can be resolved. Importantly, a gradual drop of the b-value from about 0.75 to below 0.6 is observed in the source region within the three years before the Iquique earthquake (Fig. 3e). This has only been reversed within the last days of the foreshock sequence. Similar drops of b-values before large megathrust earthquakes have been recently documented, in particular for the M9 Tohoku event¹⁵.

To reveal potential changes of background seismic activity related to aseismic processes, we fit the foreshock seismicity by means of an Epidemic-Type-Aftershock-Sequence (ETAS) model¹⁶ identifying only 42% of pre-mainshock events as Omori-type aftershocks triggered by larger foreshocks. Using the Akaike information criterion¹⁷, the remaining background rate is found to be significantly time-dependent: We identify four subsequent time periods of almost constant background rates (Fig. 3d,e). The mainshock preparation process seems to be initiated by a relative seismic quiescence, which started at the same time when b-values are found to drop and ended in July 2013, when the background rate returned to approximately the pre-quiescence values; the final phase started 18 days before the quake when the background seismicity increased by a factor of more than 35 in conjunction with the onset of the final transient GPS-signal.

Such a sequence of seismic quiescence, recovery and acceleration of background activity is expected in the stress accumulation framework ¹⁸. Based on the inverted ETAS parameters and the low b-values before the mainshock, the seismicity is expected to accelerate with time due to a branching ratio, i.e. the average number of daughter events per earthquake, larger than one indicating a transient supercritical state ¹⁹. Hence, the period leading to the Iquique earthquake documents progressive asperity failure, here observed with unprecedented detail.

An increase of foreshock activity preceding subduction megathrust events has repeatedly been reported^{18,20,21}. In contrast to, e.g., the foreshocks of the 2011 M9 Tohoku-Oki earthquake²¹, which started about three weeks prior the mainshock, the foreshock clusters described here have been active since the start of our observations in 2007. However, only more recently foreshocks with increasing magnitudes and thus more fertile aftershock sequences resulted in a supercritical state with self-accelerating seismicity¹⁹. This ultimately allowed an earthquake to nucleate that was strong enough to break into the stronger locked and thus aseismic part of the interface. From the spatial correlation of foreshock activity and slip gradients with the Iquique main shock rupture region we infer gradual unlocking of the plate interface. Moreover, the start of the b-value decrease c. 3 years ago in spite of constant plate convergence and loading rate indicates physical change at the plate interface. From only intermediate locking the Iquique segment appears to have been dominated by mostly smaller locked asperities embedded in a conditionally stable environment assuming rate and state frictional behavior is controlling locking and creep^{22–24}. Progressive rupturing of the smaller asperities by foreshocks will have loaded the remaining larger asperities in this zone until their subsequent failure: this evolution may be seen as the culmination of a run-away process as the likely key mechanism leading up to the Iquique earthquake. Both rupture direction and speed of the mainshock and its triggered large aftershock are controlled by the stress gradient in the remaining asperities corroborating theoretical analysis²⁵. This indicates that not only the size of larger asperities, but also their stress topography is important to understand the propagation, acceleration and stopping of megathrust earthquakes. The Iquique event broke a region of heterogeneous coupling, where rupture not only broke a moderate sized asperity but also penetrated into a weakly coupled zone, possibly by dynamic weakening²⁶.

Earthquake swarms preferentially occur in regions of low interseismic strain accumulation, which tend to delimit subsequent ruptures of plate interface zones²⁷. The Mw 7.7 Tocopilla earthquake with its aftershocks and the Mw 8.1 Iquique earthquake with its foreshocks might

be considered similar features. They embrace the rims of a 250 km long highly locked zone in the center of the Northern Chile Southern Peru gap with an accumulated slip deficit⁸ of some 8-9 m since 1877. Estimating the moment deficit for the entire seismic gap yields the potential for an earthquake with a maximum magnitude of Mw≈8.9 (Fig. 1) for the historically less likely case that the entire zone fails in a single event. However, the reduction of the slip deficit by about 50% in the Iquique earthquake area (Fig. 1) decreases the probability of a future earthquake releasing the whole remaining slip deficit at once. As the slip deficit reduction is only partial, though, this region will not necessarily act as a barrier such that the seismic potential of this area remains high.

- 1. Comte, D. & Pardo, M. Reappraisal of great historical earthquakes in the northern Chile and southern Peru seismic gaps. *Nat. Hazards* **4,** 23–44 (1991).
- 2. Chlieh, M. *et al.* Interseismic coupling and seismic potential along the Central Andes subduction zone. *J. Geophys. Res.* **116**, 1–21 (2011).
- 3. Ruegg, J. C. *et al.* The Mw = 8.1 Antofagasta (North Chile) Earthquake of July 30, 1995: First results from teleseismic and geodetic data. *Geophys. Res. Lett.* **23**, 917–920 (1996).
- 4. Chlieh, M. *et al.* Crustal deformation and fault slip during the seismic cycle in the North Chile subduction zone, from GPS and InSAR observations. *Geophys. J. Int.* **158**, 695–711 (2004).
- 5. Pritchard, M. E. *et al.* Geodetic, teleseismic, and strong motion constraints on slip from recent southern Peru subduction zone earthquakes. *J. Geophys. Res.* **112**, 1–24 (2007).
- 6. Delouis, B., Pardo, M., Legrand, D. & Monfret, T. The Mw 7.7 Tocopilla Earthquake of 14 November 2007 at the Southern Edge of the Northern Chile Seismic Gap: Rupture in the Deep Part of the Coupled Plate Interface. *Bull. Seismol. Soc. Am.* **99**, 87–94 (2009).
- 7. Schurr, B. *et al.* The 2007 M7.7 Tocopilla northern Chile earthquake sequence: Implications for along-strike and downdip rupture segmentation and megathrust frictional behavior. *J. Geophys. Res.* **117**, 1–19 (2012).
- 8. Métois, M. *et al.* Revisiting the North Chile seismic gap segmentation using GPS-derived interseismic coupling. *Geophys. J. Int.* (2013). doi:10.1093/gji/ggt183

- 9. Krüger, F. & Ohrnberger, M. Tracking the rupture of the Mw = 9.3 Sumatra earthquake over 1,150 km at teleseismic distance. *Nature* **435**, 937–939 (2005).
- 10. Rössler, D., Krüger, F., Ohrnberger, M. & Ehlert, L. Rapid characterisation of large earthquakes by multiple seismic broadband arrays. *Nat. Hazards Earth Syst. Sci.* **10**, 923–932 (2010).
- 11. Lay, T., Yue, H., Brodsky, E. E. & An, C. The 1 April 2014 Iquique, Chile, Mw 8.1 earthquake rupture sequence. *Geophys. Res. Lett.* **41**, 3818–3825 (2014).
- 12. Yagi, Y. *et al.* Rupture process of the 2014 Iquique Chile Earthquake in relation with the foreshock activity. *Geophys. Res. Lett.* **41**, 1–6 (2014).
- 13. Béjar-Pizarro, M. *et al.* Andean structural control on interseismic coupling in the North Chile subduction zone. *Nat. Geosci.* 1–6 (2013). doi:10.1038/NGEO1802
- 14. Schorlemmer, D., Wiemer, S. & Wyss, M. Variations in earthquake-size distribution across different stress regimes. *Nature* **437**, 539–42 (2005).
- 15. Nanjo, K. Z., Hirata, N., Obara, K. & Kasahara, K. Decade-scale decrease in b value prior to the M 9-class 2011 Tohoku and 2004 Sumatra quakes. *Geophys. Res. Lett.* **39**, (2012).
- 16. Ogata, Y. Statistical Models for Earthquake Occurrences and Residual Analysis for Point Processes. *J. Am. Stat. Assoc.* **83**, 9–27 (1988).
- 17. Marsan, D., Prono, E. & Helmstetter, A. Monitoring Aseismic Forcing in Fault Zones Using Earthquake Time Series. *Bull. Seismol. Soc. Am.* **103**, 169–179 (2013).
- 18. Mignan, A. Seismicity precursors to large earthquakes unified in a stress accumulation framework. *Geophys. Res. Lett.* **39**, (2012).
- 19. Helmstetter, A., Kagan, Y. Y. & Jackson, D. D. Importance of small earthquakes for stress transfers and earthquake triggering. *J. Geophys. Res.* **110**, 1–13 (2005).
- 20. Bouchon, M., Durand, V., Marsan, D., Karabulut, H. & Schmittbuhl, J. The long precursory phase of most large interplate earthquakes. *Nat. Geosci.* **6,** 299–302 (2013).
- 21. Kato, A. *et al.* Propagation of slow slip leading up to the 2011 Mw 9.0 Tohoku-Oki earthquake. *Science* **335**, 705–708 (2012).
- 22. Scholz, C. H. Earthquakes and friction laws. *Nature* **391**, 37–42 (1998).
- 23. Bilek, S. L. & Lay, T. Tsunami earthquakes possibly widespread manifestations of frictional conditional stability. *Geophys. Res. Lett.* **29**, 1–4 (2002).
- 24. Kaneko, Y., Avouac, J. P. & Lapusta, N. Towards inferring earthquake patterns from geodetic observations of interseismic coupling. *Nat. Geosci.* **3**, 363–369 (2010).
- 25. Das, S. & Kostrov, B. V. Breaking of a Single Asperity: Rupture Process and Seismic Radiation. *J. Geophys. Res.* **88,** 4277–4288 (1983).

- 26. Noda, H. & Lapusta, N. Stable creeping fault segments can become destructive as a result of dynamic weakening. *Nature* **493**, 518–521 (2013).
- 27. Holtkamp, S. & Brudzinski, M. R. Megathrust earthquake swarms indicate frictional changes which delimit large earthquake ruptures. *Earth Planet. Sci. Lett.* **390**, 234–243 (2014).
- 28. Dorbath, L., Cisternas, A. & Dorbath, C. Assessment of the size of large and great historical earthquakes in Peru. *Bull. Seismol. Soc. Am.* **80**, 551–576 (1990).

Acknowledgements Data used in this study come from the IPOC initiative (www.ipocnetwork.org) operated by GFZ German Research Centre for Geosciences, Institut de Physique du Globe de Paris (IPGP), Centro Sismológico National, Universidad de Chile, and Universidad Cátolica del Norte, Antofagasta, Chile. We also acknowledge the French-Chilean LIA 'Montessus de Ballore' and USA-Chilean Central Andean Tectonic Observatory Geodetic Array projects for giving access to data of several of their cGPS stations in Chile. Part of this work was made possible by the Hazard Assessment and Risk Team (HART) initiative funded by GFZ and Hannover Re.

Author Contributions: BS processed the entire seismicity of the IPOC network set up by GA, SB, JV and BS. SH performed the ETAS- and b-value analysis. RW, YZ and TD contributed the coseismic slip models. MP and FT performed the backprojection analysis. MB was responsible for the GPS data processing. JB, AH and MM analyzed geodetic locking and slip transients. AH modeled the accumulated, released and remaining moment. PV compiled the historical earthquake record, and OO wrote major parts of the mechanical interpretation.

Author Information: Reprints and permissions information is available at www.nature.com/reprints. The authors declare no competing financial interests. Correspondence and requests for materials should be addressed to B.S. (schurr@gfz-potsdam.de).

Figure legends:

Fig. 1: Map of Northern Chile and Southern Peru showing historical earthquakes and instrumentally recorded megathrust ruptures. IPOC instruments used in the present study (BB: broadband; SM: strong motion) are shown as blue symbols. Left panel shows historical^{1,2} and instrumental earthquake record. Rupture length was calculated using the regression suggested by Dorbath²⁸, with grey lines for earthquakes M>7 and red lines for Mw>8. Color coded is the slip distribution of the 2014 Iquique event and its largest aftershock derived in this study, with contour intervals of 0.5 m. Green and black vectors are observed and modelled horizontal surface displacements of the mainshock. Slip area of most recent

other large ruptures^{4,5,7} are also plotted. Right panel indicates moment deficit per km along strike left along plate boundary after the Iquique event for moment accumulated since 1877 assuming current locking (Fig. 3a). Total accumulated moment since 1877 from 17-25°S is 8.97, remaining moment after subtracting all earthquake events with Mw>7 is 8.91 for the entire Northern Chile Southern Peru seismic gap.

Fig. 2: Kinematic rupture development of the Mw 8.1 main and Mw 7.6 aftershock and distribution of fore- and aftershocks. The nucleation point of both earthquake ruptures is indicated by coloured stars. **(a)** Arrows indicate the propagation of main energy release during the first 40s and 25s, respectively. The contour lines represent isolines of slip rate for the mainshock from the kinematic inversion during different time intervals after rupture nucleation (0.05 m/s intervals, line thickness scaled by slip-rate). Coloured diamonds represent maxima of semblance scaled to the peak value of the emitted energy for main and aftershock for each time step based on the backprojection of teleseismic waveforms. **(b)** Moment rate and time history of backprojected energy (arbitrary absolute scale). **(c)** Map and longitudinal cross section of c. 3600 fore- and c. 1400 aftershocks coloured according to their time of occurrence relative to the mainshock. The slip of the main- and largest aftershock is contoured. The beachball depicts the double-couple of the largest Mw 6.7 foreshock that had a rupture geometry distinctively different from the main and largest aftershock (Fig. 1) and a centroid depth of only 9 km (blue star) and thus probably has occurred in the upper plate.

Fig. 3: Maps of interseimic locking and b-value and time history of seismicity and deformation. (a) Geodetic interseismic locking and foreshocks. The July-August 2013, January and March 2014 foreshock clusters are marked. (b) The b-value map of central portion of Northern Chile gap for the last 2000 days before the main shock, where results are calculated for all M3+ foreshocks within a 50 km distance if their number exceeds 100. The

rectangular box encloses the area used for the results in plots c, d, and e. (c) Magnitude versus time plot. Arrows mark the July/August 2013, January 2014 and March 2014 clusters. (d) Observed and ETAS-modeled cumulative M3+ activity, where coloured lines are fits of the estimated background for the 4 phases, during each of which the background rate is almost constant (see text). Inset shows measured GPS displacement time-series stacked from near-coast stations between 19-21°S smoothed with a 4-day moving-average and the modelled signal related to cumulative slip of the foreshock events. (e) b-value (+uncertainties) time series for the events inside the box (colored and grey shaded area). Black crosses and bars refer to the results for the events outside the box.

Methods

1 Kinematic source inversion

Kinematic slip inversions were made for the Mw 8.1 April 1st mainshock and the Mw 7.6 April 3rd aftershock, respectively. For each earthquake we first inverted the static 3-component GPS displacement data for the final fault slip and then teleseismic and local strong-motion waveforms for the time-dependent kinematic rupture process. Finally we performed a joint inversion of the waveform and GPS data.

The teleseismic data (P waveforms on the vertical component) were selected from a set of broadband stations (18 for the mainshock and 17 for the aftershock) with a good azimuth and distance coverage (see Extended Data Fig. 1c). In addition seismograms from 20 3-component strong-motion seismographs were used. Both teleseismic and local waveform data were converted to velocity and filtered with a 0.01-0.1 Hz band-pass. The static displacement data were gleaned from 21 continuous GPS stations, most of which are co-located with the strong-motion stations. In the joint inversions, the GPS and seismic waveform data sets were weighted equally.

For the inversion we used a linear approach implemented by Zhang et al.²⁹, in which multiple time windows are used for describing the sub-fault source time functions. The fault geometry for the two earthquakes was adopted from the Slab1.0 model³⁰. The sub-fault size ranges between 10 and15 km. Synthetic Green's functions were calculated with the code of Wang³¹ based on the seismic reference earth model AK135³² modified with the local 1D crust structure from the CRUST 2.0 model³³.

Extended Data Fig. 1a shows the final slip distribution for the mainshock of April 1st, which is characterized by a single asperity with the lower edge just below the coastline. This result is robust, showing similar slip distribution with and without the constraint from the static GPS displacement data. However, the temporal development of the rupture features two sub-

events, as shown by Extended Data Animation 1a. The rupture was initiated in the foreshock region (Fig. 2 and 3) and propagated in the south-downdip direction along the maximum locking gradient during the first 40-50 s (1. peak in source-time-function (STF)). Then the region near the hypocenter seems to become reactivated and the rupture propagated towards the north-downdip and updip directions simultaneously (2. peak STF). The observed and modeled teleseismic and strong-motion seismograms are shown in Extended Data Fig. 1c.

Similarly, Extended Data Fig. 1b and Extended Data Animation 1b show the kinematic results for the aftershock of April 3. This aftershock extended the mainshock rupture further in the southeast-downdip direction and crossed the coastline near the city of Iquique. Its slip distribution is rather compact, despite a quite complicated STF.

2 Backprojection

In the backprojection analysis, the source position of the seismic radiation is inferred by projecting the seismic wavefront of ground velocity recorded by an array of stations at teleseismic distances onto the source region^{9,34}. The source location is chosen as the area in the source region leading to the best overlap between the traces.

We have backprojected the radiation emitted in the frequency band 1-4 Hz (filtered by a zero-phase 4th-order Butterworth filter) dividing the rupture process in time windows of 8 sec, sliding with an overlap of 6 sec. We have used stations from the continental USA (mostly from TA and N4 networks, www.usarray.org) and have searched the source over a grid in the range 18°-21°S and 69°W-71°W with a spacing of 0.05°.

We have measured the coherence between the traces by semblance^{10,35}, which is a normalized version of the stacked energy and ranges in the interval [0-1], where S=1 signifies perfectly coherent signals. Semblance and energy at the i-th grid point in the source area are defined as follows:

$$S_{i}(t) = \frac{1}{N} \frac{\int_{-L/2}^{L/2} |\sum_{k=1}^{N} \bar{u}_{k} (t - t_{ik} - t')|^{2} dt'}{\int_{-L/2}^{L/2} \sum_{k=1}^{N} \bar{u}_{k} (t - t_{ik} - t') dt'}$$

$$E_{i}(t) = \frac{1}{N} \int_{-L/2}^{L/2} \left| \sum_{k=1}^{N} u_{k} (t - t_{ik} - t') \right|^{2} dt'$$

where $u_k(t)$ is the continuous trace of the k-th station, and $\bar{u}_k(t)$ is the continuous trace normalized to its maximum absolute value during each time window, N is the number of sensors, t_{ik} is the travel time from the i-th grid cell to the k-th station, and the time integral is over the analysis window (L).

The travel times are those predicted by a 1D global velocity model plus a site-based correction:

$$t_{ik} = t_{ik}^{1D} + \Delta t_k^s$$

where t_{ik}^{1D} is the travel time from the i-th grid point to the k-th sensor predicted by ak135 velocity model³² and Δt_k^s is a static correction associated with each station. Δt_k^s has been estimated as the mean value of the residual time-shifts between one station and all the others after removing the travel times predicted by the 1D model between each station and the hypocenter provided by GEOFON (70.82°S 19.64°W). The residual time-shifts between the stations have been calculated maximizing the cross-correlation of the first 8 sec of the mainshock (filtered in the band 0.4-3 Hz) between all the possible stations pairs. Only stations with mean cross-correlation higher than 0.8 have been selected, leading to a set of 310 stations adopted for the backprojection analysis. The same set of static corrections has been adopted for both the mainshock and the aftershock.

The time development of semblance and energy is shown in Extended Data Figure 2a and 2b. Extended Data Animations 2a and 2b give an impression of the propagation of rupture energy.

In Extended Data Figure 2c we quantify the rupture speed along a down-dip profile on the rupture plane.

3 Interseismic locking

While models of interseismic coupling for this region exist^{2,8,13} it is in the interest of consistency to produce a locking model on the same geometry as used for the coseismic slip modelling. We took the ITRF08 GPS velocities data of Métois et al.⁸ and performed our own corrections to fix velocities to a stable South American reference frame, and to correct for overlapping tectonic signals of shortening and sliver motion.

The GPS velocities in this region are not ready to use in the inversion because they are contaminated by the Andean sliver motion² and shortening^{36,37}. Métois et al.⁸ decontaminated the velocities by applying a single Euler pole correction on the craton-fixed velocity field. In a similar approach, we applied a series of Euler pole corrections in the following way. First we translated Métois' ITRF08 velocities into a stable South American reference frame by inverting for the Euler of the rotation of several South American reference stations and applying this Euler pole rotation correction (29.9°S, 115.9°W, -0.12°/Ma) to the ITRF08 velocities. Next we applied a correction for the forearc sliver motion by means of another Euler pole correction. The sliver correction Euler pole (2.4°S, 80.3°W, -0.16°/Ma) was calculated for the misfits between data and modelled displacements for a smooth backslip model fully locked from the trench to the coastline. This sliver correction was applied to all the stations in the network. Finally, shortening corrections were applied to the data at selected stations where the misfit between the highly smoothed locked model displacements and the sliver corrected data was highest. Shortening corrections for stations in the North-East of our model were rotated about Euler pole of 14.9°S, 72.4°W at 0.50°/Ma. Shortening corrections for stations in the South of our model were rotated about Euler pole of 14.6°S, 79.4°W at 0.12°/Ma. The sliver and shortening corrections can be seen in Extended Data Figure 3a. Interseismic coupling is modelled with the backslip method. In this modelling scheme the

surface displacements due to subduction are modelled as dislocations (backslips) on the plate interface, with regions of largest modelled dislocation interpreted as being the most locked regions. For forward modelling, we use a layered elastic half space and IASP Earth model³⁸. The Green's functions are computed using code PSGRN/PSCMP³⁹, the geometry consists of 15x90 rectangular subfaults with an average edge length of about 13 km and follows the depth of SLAB1.0³⁰. The inversion is a weighted damped least squares scheme⁴⁰, data are weighted according to estimated accuracies. The inversion scheme uses steepness as smoothing operator in the design matrix taking into account the size and center distance between neighboring patches to avoid distortion of the solution. The optimal smoothing factor is found based on an L-curve plot as shown in Extended Data Figure 3c used as a basis for locking shown in Extended Data Figure 3d. Checkerboard test were performed to assess the resolving power of the inversion (Extended Data Figure 3e). Based on the locking map, we computed the accumulated moment since the 1877 Mw=8.8 earthquake, assuming that the locking was constant at the same level as at present (Extended Data Figure 3b).

4 Characterizing transient signals in the data

The excellent spatial coverage and proximity of the cGPS network near to the mainshock hypocentre enabled us to analyze the kinematics of the plate interface leading up to the mainshock testing for prior slip and its relationship to the foreshocks. To see any transient signals we first de-trended the time series (obtained by the processing detailed in section 6) from the long-term constant deformation due to plate convergence and removed spurious noise. The de-trended time series still contain considerable network-correlated noise, particularly since mid-2013. We suppressed this noise using the common mode filtering approach⁴¹, whereby we selected stations distant from the source region and averaged their de-trended signals. This signal has been subtracted from the de-trended time series at our stations of interest. Finally a moving average of 8 days is applied to the data to smooth the

remaining spurious fluctuations. Extended Data Figure 4a shows the stations of interest (closest to the Mw=8.1 and Mw=7.6 hypocentres) and the selection of stations used to average the network-correlated noise. Generally the common mode filter seems to work reasonably well and brings the de-trended time series within noise fluctuations back to the de-trended line (y=0), but in some cases the filter over/under-corrects. The filter is better constrained, and therefore performs better for epochs when we have fuller station coverage. From the corrected time series (Extended Data Figure 4b) we can see that transient slip started in early-January 2014, although at some stations the amplitude for the beginning of this transient signal is not higher than the background noise amplitude earlier in the signal. Perhaps the most convincing argument for the case of the early-January transient being a real signal is found when we plot the de-trended time series with increasing time in plan view (Extended Data Figure 4c and Extended Data Animation 5). The suspected signal is distinct from noise seen earlier than 2014 in that the vectors point towards a common location, as we would expect as a response for a source of slip on the plate interface. Furthermore, the timing of the transient coincides with the January 2nd foreshock cluster, and the GPS vectors are pointing towards the location of this cluster. Furthermore, from Extended Data Animation 5 we can see that the displacement associated with the early January cluster is permanent: The azimuths of the southern stations varied wildly before this cluster, whereas following the cluster the azimuths consistently point towards the cluster location. From this result one could suggest that the foreshock activity on the plate interface is mechanically related to plate interface slip in the immediate vicinity. However, the temporal smoothing due to the application of a moving average filter means that one cannot say which process (earthquakes or cGPS transient) starts first, or whether they are coeval. The largest transient signal begins with the onset of the Mid-March foreshock cluster and continues until the eventual rupture of the Mw=8.1 event of April 1st. This second transient is clearly a real signal due to the large

signal to noise ratio and again because the vectors of the GPS point towards the foreshock cluster region.

Having established these transients we can test whether they are explained by coseismic displacements of the foreshocks, or by aseismic slip. Included in Extended Data Figure 4 and Extended Data Animation A3 are the seismic displacements predicted at the GPS stations by forward modelling the scaling relation-derived slip for each foreshock in the catalogue, and an assumed rake in the direction opposite to plate convergence. For consistency, the seismic predictions have been smoothed with the same time window as for the data. The evolution of seismic displacement in early January closely matches that of the GPS both in pattern and magnitude. The GPS vectors are then interrupted by noise until we get to the second cluster in mid-March. Cumulative GPS data and seismic predictions at the time of the second cluster are also closely matching in magnitude. Considering the uncertainties involved in the seismic displacement predictions and the noise of the GPS, the remarkable similarity in cumulative displacement between data and prediction points to the scenario of a mostly seismic release of slip on the plate interface leading up to the Mw=8.1 mainshock.

5 Earthquake catalogue production and analysis

We analyzed the earthquake catalog within latitude18.0S-23.0S and longitude 69.8W-73.0W since 1/1/2007 including the M8.1 Pisagua earthquake and its first ten days of aftershocks. The catalogue was produced with a multistage automatic procedure applied to stations from the IPOC network and a few additional long-term temporary stations. We used first detections from a short-term versus long-term average ratio (STA/LTA) trigger and a grid search algorithm for event association and preliminary locations and then specialized P and S phase pick algorithms on targeted phase windows for an improved set of phase picks, which were jointly inverted for new hypocentres and station-phase terms using a 1D velocity model developed for the Chilean forearc⁴². At each step, quality checks were performed to weed out

spurious picks, wrong associations, and false and badly constrained events. Finally the catalogue was relocated using the double-difference algorithm⁴³. The procedure is described in detail in ref. ⁴⁴. Magnitudes are local magnitudes (MI) utilizing a standard attenuation relation for California. MI calculated in this way has been found to overestimate the size of moderate and larger events in northern Chile for which Mw is available. The catalogue consists of 16613 events before and 1377 events after the mainshock with local magnitudes above 1.2. For our detailed analysis, we focused on a box between latitude17.0S-21.0S and longitude 70.0W-72.0W enclosing the source region of the mainshock with 3187 M>1.2 foreshocks and 1284 M>1.4 aftershocks (available as Source Data table). The corresponding magnitude distributions are shown in Extended Data Figure 5.

Earthquake catalogues are known to be incomplete towards small magnitudes, in particular directly after large earthquakes⁴⁵. To avoid effects of incomplete detections, we used a cutoff magnitude of M_c =3 which is – to be conservative – well above the completeness value of 2.6 estimated by the maximum curvature method inside the box⁴⁶. In the case of the b-value map shown in Fig. 3b of the main article, we calculated b-values only on grid nodes where the completeness estimator yields a value lower or equal to 3. However, after larger earthquakes, catalogs are generally lacking also $M > M_c$ events for a short time, because the mainshock coda and overlapping aftershocks limit the detection ability. The time period with incomplete detection is a function of the mainshock magnitude M and cutoff magnitude M_c and has been found to be well fitted by the functional form $\log(\Delta t) = (M - M_c - c_1)/c_2$ similarly to California seismicity⁴⁷, but with slightly different parameters $(c_1 = 5.2$ and $c_2 = 1.5$). We ignored those incomplete time periods in our analysis of b-values as well as in the ETAS modeling. The corresponding frequency-magnitude distributions are shown by bold lines in Extended Data Figure 5a.

The b-values are calculated by the maximum likelihood method according to

$$b = \frac{1}{\log(10)\left[\overline{m} - M_c - \Delta M/2\right]}$$

with \overline{m} being the mean magnitude and ΔM the bin width of the magnitudes in the catalog (0.1 in our case)⁴⁸ and the standard deviation of the b-value estimation is calculated according to Shi & Bolt⁴⁹. The results are shown in Fig. 3e of the main article. In Extended Data Figure 5b we additionally present the corresponding frequency-magnitude distributions at different times. Note that the time refers to the average time of 200 subsequent events.

The ETAS model is also fitted by maximum likelihood method, where we applied a method to estimate transient background rates developed recently by Marsan et al.¹⁷ and further tested by Hainzl et al.⁵⁰. Earthquake catalogs are usually dominated by aftershock activity which hinders the detection of changes of background activity related to aseismic processes. Thus we try basically to decluster the earthquake catalog to recover this forcing signal. The method is based on the inversion of the empirical ETAS-model in which the earthquake R is determined by summation of a background rate μ and ongoing Omori-type aftershock activity from precursory earthquakes,

$$R(t) = \mu(t) + \sum_{i:t_i < t} K e^{\alpha(M-M_t)} / (c+t-t_i)^p,$$

with parameters c and p related to the temporal decay and K and α to the aftershock productivity relation for empirically observed aftershocks. While the background rate is constant in the original model¹⁶, it is allowed to vary in time in the new approach to account for aseismic transients. However, smoothing of the background rates in time is crucial to avoid overfitting, where the optimal smoothing is determined by the Akaike information criterion.

While all M2.5+ earthquakes are used to calculate R(t), we optimize the parameters and background rate only for M3+ events in completely recorded time intervals (see above). Furthermore, we start the optimization time window not before 2000 days prior to the

mainshock to minimize the effect of missing historic activity. Our approach yields the aftershock parameters c=0.012 days, p=1.13, K=0.0048, and α =1.87, which are in the range of typical values observed in previous studies. Depending on the b-value and the maximum magnitude, the branching ratio n, which is the average number of daughter events per earthquake, can be calculated¹⁹. Our b-value estimates show a decrease of b-values from about 0.8 to 0.6 before the mainshock, which corresponds to an increase of the branching ratio from 0.62 (0.75) to 1.86 (3.14) for M_{max} =8.0 (9.0). For n<1, the system is in a subcritical state where sequences will decay with time. For n>1, the system is in a supercritical state, where the activity will start to self-accelerate with time which obviously can be only of transient nature¹⁹. We find that the source region of the Pisagua earthquake seemed to move gradually from a subcritical into a supercritical state while approaching the mainshock time.

The revealed time-dependent background rate explains about 60% of the observed foreshock activity and can be well fitted by four time periods with constant activity. These periods are characterized by change points at time 1150, 250 and 18 days before the mainshock separating an initial phase, a relative quiescence, a recovery phase and a final phase of strong forcing. The corresponding background rates are 0.22 M3+ events per day in the time period [2000-1150] days; 0.14 M3+ events per day in the relative quiet time period [1150-250] days; 0.28 M3+ events per day in the time period [250-18] days; and 10 M3+ events per day in the time period in the last 18 days. To determine the significance of these rate changes we calculated the Z-values⁵¹. We find that all rate changes are significant with |Z|=4.1, 3.9, and 12.5 for the changes at 1150, 250 and 18 days before the mainshock, respectively.

6 GNSS data processing strategy

All processing of GNSS data was done with Bernese GNSS Software Version 5.2⁵². For the preseismic position time series sites from 63° to 74° W and 16° to 25° S were selected. The

processing starts on January 1, 2008 and continues until April, 20, 2014. Overall there are 50 stations included. Daily solutions are generated using the final satellite orbits and earth orientation parameters from CODE (Center of Orbit Determination Bern). All parameters are derived from a least-squares adjustment using double difference phase observations. GPS as well as GLONASS observations have been used. Absolute corrections for antenna phase center offsets and phase center variations for receivers and satellites⁵³ associated to the latest realization of the International Terrestrial Reference Frame ITRF2008 were applied. Ocean loading corrections are derived from ocean tide model FES2004⁵⁴. An elevation cut-off angle of 5° and a sampling rate of 30 seconds have been used. The dry and wet part of troposphere were calculated using the GMF⁵⁵. While the dry part is taken *a priori* from the model the wet coefficients are estimated with a temporal resolution of 1 hour. To align the sites to stable South America sites on the rigid plate have to be selected ideally far away from the location of the Pisagua event. Due to data gaps there is only a small number of sites matching these requirements. Here only the stations in Arequipa, Peru (areq) and Cordoba, Argentina (unsa) cover the whole time span of processing. For the coseismic displacements exactly the same strategy as for the daily solutions was used. The displacements are the difference between the static coordinates from one day before and after the event excluding data during the event.

References:

- 29. Zhang, Y. *et al.* The 2009 L'Aquila Mw 6.3 earthquake: a new technique to locate the hypocentre in the joint inversion of earthquake rupture process. *Geophys. J. Int.* **191**, 1417–1426 (2012).
- 30. Hayes, G. P., Wald, D. J. & Johnson, R. L. Slab1 .0: A three-dimensional model of global subduction zone geometries. *J. Geophys. Res.* **117**, 1–15 (2012).
- 31. Wang, R. A Simple Orthonormalization Method for Stable and Efficient Computation of Green's Functions. *Bull. Seismol. Soc. Am.* **89,** 733–741 (1999).
- 32. Kennett, B. L. N., Engdahl, E. R. & Buland, R. Constraints on seismic velocities in the Earth from travel times. *Geophys. J. Int.* **122**, 108–124 (1995).

- 33. Bassin, C., Laske, G. & Masters, G. The Current Limits of Resolution for Surface Wave Tomography in North America. *Eos, Trans. AGU* **81,** F897 (2000).
- 34. Ishii, M., Shearer, P. M., Houston, H. & Vidale, J. E. Extent, duration and speed of the 2004 Sumatra-Andaman earthquake imaged by the Hi-Net array. *Nature* **435**, 933–936 (2005).
- 35. Neidell, N. & Taner, M. Semblance and other coherency measures for multichannel data. *Geophysics* **36**, 482–497 (1971).
- 36. Brooks, B. A. *et al.* Orogenic-wedge deformation and potential for great earthquakes in the central Andean backarc. *Nat. Geosci.* **4,** 380–383 (2011).
- 37. Allmendinger, R. W., González, G., Yu, J., Hoke, G. & Isacks, B. Trench-parallel shortening in the Northern Chilean Forearc: Tectonic and climatic implications. *Geol. Soc. Am. Bull.* **117**, 89 (2005).
- 38. Kennett, B. L. N. & Engdahl, E. R. Traveltimes for global earthquake location and phase identification. *Geophys. J. Int.* **105**, 429–465 (1991).
- 39. Wang, R., Lorenzo-Martín, F. & Roth, F. PSGRN/PSCMP—a new code for calculating co- and post-seismic deformation, geoid and gravity changes based on the viscoelastic-gravitational dislocation theory. *Comput. Geosci.* **32**, 527–541 (2006).
- 40. Menke, W. Geophysical data analysis: discrete inverse theory. (Academic Press, 2012).
- 41. Wdowinski, S., Bock, Y., Zhang, J., Fang, P. & Genrich, J. Southern California Permanent GPS Geodetic Array: Spatial filtering of daily positions for estimating coseismic and postseismic displacements induced by the 1992 Landers earthquake. *J. Geophys. Res.* **102**, 57–70 (1997).
- 42. Husen, S., Kissling, E., Flueh, E. & Asch, G. Accurate hypocentre determination in the seismogenic zone of the subducting Nazca Plate in northern Chile using a combined on-/offshore network. *Geophys. J. Int.* **138**, 687–701 (1999).
- 43. Waldhauser, F. & Ellsworth, W. L. A double-difference earthquake location algorithm: method and application to the northern Hayward fault, California. *Bull. Seismol. Soc. Am.* **90**, 1353–1368 (2000).
- 44. Sippl, C. *et al.* Geometry of the Pamir-Hindu Kush intermediate-depth earthquake zone from local seismic data. *J. Geophys. Res. Solid Earth* **118**, 1438–1457 (2013).
- 45. Kagan, Y. Short-term properties of earthquake catalogs and models of earthquake source. *Bull. Seismol. Soc. Am.* **94,** 1207–1228 (2004).
- 46. Woessner, J. & Wiemer, S. Assessing the quality of earthquake catalogues: Estimating the magnitude of completeness and its uncertainty. *Bull. Seismol. Soc. Am.* **95**, 684–698 (2005).

- 47. Helmstetter, A., Kagan, Y. & Jackson, D. Comparison of short-term and time-independent earthquake forecast models for southern California. *Bull. Seismol. Soc. Am.* **96**, 90–106 (2006).
- 48. Marzocchi, W. & Sandri, L. A review and new insights on the estimation of the b-value and its uncertainty. *Ann. Geophys.* **46**, 1271–1282 (2003).
- 49. Shi, Y. & Bolt, B. The standard error of the magnitude-frequency b value. *Bull. Seismol. Soc. Am.* **72,** 1677–1687 (1982).
- 50. Hainzl, S., Zakharova, O. & Marsan, D. Impact of Aseismic Transients on the Estimation of Aftershock Productivity Parameters. *Bull. Seismol. Soc. Am.* **103**, 1723–1732 (2013).
- 51. Habermann, R. E. *Precursory seismicity patterns: Stalking the mature seismic gap in Earthquake prediction An international review.* 29–42 (American Geophysical Union, 1981).
- 52. Dach, R., Hugentobler, U., Fridez, P. & Meindl, M. *Bernese GPS software version 5.0. User manual. Astron. Institute, Univ. Bern* **640**, 640 (2007).
- 53. Dach, R. *et al.* Improved antenna phase center models for GLONASS. *GPS Solut.* **15**, 49–65 (2011).
- 54. Lettelier, T. Etude des ondes de marée sur les plateaux continentaux. 237p (2004).
- 55. Boehm, J., Niell, A., Tregoning, P. & Schuh, H. Global Mapping Function (GMF): A new empirical mapping function based on numerical weather model data. *Geophys. Res. Lett.* **33**, L07304 (2006).

Extended Data Figure Legends

Extended Data Figure 1: Slip inversion scenarios employing different data sets and final waveform fits. (a) Final slip distribution of the April 1 mainshock obtained from the waveform inversion (left) of the teleseismic and local strong-motion seismograms, the inversion (middle) of static GPS displacement data, and the joint inversion (right) of the waveform and GPS data. (b) Same for the April 3 aftershock. (c) Data fit of the joint kinematic inversion for the April 1 mainshock. Top: Observed and modeled teleseismic P waveforms. Station codes are marked on seismogram and on map. Bottom: Comparison between the observed and modeled local strong-motion waveforms. Traces are scaled to a common maximum in each sub-plot. Right: Same for the April 3 aftershock.

Extended Data Figure 2: Source time history and rupture velocity estimation from backprojection of high frequency teleseismic waves. Time history of (a) the peak semblance at each time frame (blue) and (b) corresponding energy (red, arbitrary units) for the mainshock (left) and the Iquique aftershock (right). Energy integrated over the whole grid is plotted as a black line. Whereas the red curves describe the energy time history of one (the principal) radiating point, the black lines take into account the seismic energy emitted from the whole source area. The time axis represents the central point of the 8 s long sliding windows, i.e. the first onset of the event will affect the energy and semblance at nominal times up to 4 s before the physical onset of rupture. The semblance and energy peak at ~160 s corresponds to an early aftershock. The area of the diamonds of Fig. 2b in the main text is scaled to the energy (red curves) displayed in the panels b) (only solutions with semblance higher than 0.05 are displayed in Fig. 2b). (c) Distance of maximal semblance peaks to a reference profile (Transect 1 and Transect 2 for the mainshock (left) and the aftershock (right), respectively, plotted in Extended Data animation 2a) and b). The figure is zoomed in the down-dip migrations of the rupture fronts (about 0-30 seconds). The accelerated propagation can be identified in the interval 15-30 s. The area of the circles is scaled to the energy of the semblance maxima (red curves of Extended Data Figure 2 b).

Extended Data Figure 3: Interseismic GPS data corrections, slip deficit estimation and sensitivity tests for interseismic locking inversion. (a) Demonstrating the effect of sliver and shortening corrections on the interseismic GPS data. Left plot shows the data in the stable South American reference frame. Red vectors indicate the stations that the corrections are applied to. All stations undergo the sliver correction. Stations in the North-East and South-East undergo shortening corrections. b) Slip deficit estimation. The left panel shows our locking model and the central panel a compilation of events since 1877 according to ref. 1 plus the Antofagasta and Tocopilla earthquakes of 1995 and 2007 (ref. 4; ref. 7), as well as our solutions for the Pisagua main shock and largest aftershock. The right panel shows

moment density along trench projected on latitude. The total accumulated moment corresponds to a magnitude 8.97 event. This is about 6 times less than was released during the 1960 Valdivia magnitude 9.5 event further south, but 6 times more than was released in our region of interest between 1877 and now according to the events listed in the central panel summing up to a magnitude of 8.41. Even though the Pisagua sequence released a significant amount of the moment in the northernmost part, the remaining moment would still correspond to a magnitude of 8.92. c) Model smoothness plotted against residual. The optimal smoothing factor of 0.05 in the corner of the L-curve resulted in a residual of 0.17 cm/y. d) A selection of solutions with different smoothing factors. The central is our preferred solution. Black lines are 1 m isolines of the coseismic slip distribution of the main shock and the largest aftershock. e) Checkerboard tests of locking. On top, forward models consisting of 3 and 2 rows of locked patches. The lower panels show inverted locking patterns using the signal from the forward models at the GPS station positions applying the same uncertainties as in the actual observation data. In case of three locking rows, the trenchward row is clearly missed, while the areas closer to the station positions (magenta) are captured fairly well, the resolution being about 40 km.

Extended Data Figure 4: Pre-seismic GPS displacement time series and maps. a) Left: Map showing stations used for common mode filtering (black triangles) and those to which the correction signal is applied (green triangles). b) East and North displacement time series of the de-trended, common-mode filtered data are plotted with blue crosses. The green lines are the cumulative GPS displacements predicted by the forward modeling of elastic displacements for events in the seismic foreshock catalogue. Black vertical dashed lines indicate the onsets of the two clusters of 2014. The red dashed line shows the zero positions of the GPS after de-trending. A significant departure of the data from this zero position is an indication of transient motion at that station. c) The two panels show the GPS data

displacements (blue) and the forward modeled GPS displacements of the seismically related slip (red) between the time periods shown above each panel. Both the data and the predictions have been smoothed with a 9-day long moving average filter. Error ellipses are shown for the data displacements. The black dashed line is the trench and the solid black lines are the coastline and political borders. Events from the foreshock catalogue for days within the specified time periods (also considering length of smoothing window) are plotted in dark grey. For the first 2014 cluster (left panel) GPS stations of interest in the south move towards a common source. For the second 2014 cluster (right panel) GPS vectors point towards the eventual Mw=8.1 rupture zone.

Extended Data Figure 5: a) The frequency-magnitude distribution of earthquakes within latitude 17.0S-21.0S and longitude 70.0W-72.0W, used in our b-value analysis and ETAS-modeling. The histogram of the overall seismicity is shown by grey boxes, while thin lines refer to the cumulative distributions of foreshocks, aftershocks and the overall activity. Bold lines refer to the data used for the analysis above the magnitude threshold (Mc=3) ignoring time-periods of incomplete recordings after larger earthquakes. **b)** Frequency-magnitude distributions at different times before the mainshock. The distributions correspond to the b-values shown in grey in Fig. 3e of the main article.

